MEASUREMENT SCIENCE REVIEW, **24**, (2024), No. 5, 174-182

sciendo

ISSN 1335-8871

MEASUREMENT SCIENCE REVIEW

Journal homepage: https://content.sciendo.com

Equivalent Mechanical Model of a Microchannel Plate

Shengdan Zhang[1,2], Yonglin Bai[1*], Weiwei Cao[1,2], Junjun Qin[1], Jiarui Gao[1], Le Chang[3], Beihong Liu[3], Zexun Hu[4], Zhujun Chu[3], Xiaoqing Cong[4], Yongwei Dong[5], Zhigang Wang[5]

[1]*Key Laboratory of Ultrafast Photoelectric Diagnostic Technology, Xi'an Institute of Optics and Precision Mechanics, Chinese Academy of Sciences, Xinxi Road, No.17, 710119, Xi'an, China,* baiyonglin@opt.ac.cn
[2]*University of Chinese Academy of Sciences, Yanxi Lake East Road, No.1, 100049, Beijing, China,* zhangshengdan@opt.ac.cn
[3]*North Night Vision Technology Co., Ltd., Hongwai Road, No.5, 650217, Kunming, China,* cl610@163.com
[4]*Nanjing Branch of North Night Vision Technology Co., Ltd., Kangping Street, No.2, 211102, Nanjing, China,* zexunhu@163.com
[5]*Institute of High Energy Physics, Chinese Academy of Sciences, Yuquan Road, No.19, 10049, Beijing, China,* dongyw@ihelp.ac.cn

Abstract: The microchannel plate (MCP) is an electron multiplier with millions of micro through-holes that must withstand strong vibrations and enormous shocks in spaceborne detectors. To ensure the reliability and robustness of the MCP in space applications, we proposed an equivalent mechanical model of the MCP to investigate its mechanical properties, since the direct creation of the finite element model using the finite element method (FEM) is not feasible. Then, we developed a test system to verify the effectiveness of the equivalent mechanical model. The results show that the error of harmonic response analysis and the test result is less than 10 %, which is acceptable. Finally, we conducted parametric studies of the MCPs and obtained the equivalent mechanical model of the MCPs with different geometric parameters. This study will help researchers to optimize the MCP for aerospace-grade detectors.

Keywords: Microchannel plate, equivalent model, finite element method, geometries, material properties.

1. INTRODUCTION

As an unprecedented facility for dark matter research, the high energy cosmic-radiation detection (HERD) facility in contrast to alpha magnetic spectrometer (AMS), dark matter particle explorer (DAMPE), etc., has unique features in terms of excellent energy detection, particle identification capability and energy resolution [1]-[3]. Therefore, one of the most critical components of the facility, the aerospace-grade image intensifier, must have superiorities such as wide dynamic range, high aerospace adaptability, low non-uniformity and low crosstalk. Therefore, it is crucial to improve the performance of the weakest component of the image intensifier – the microchannel plate (MCP).

The MCP for spaceborne detectors is a type of multiplier used to capture electrons, ions, photons, X-rays and other particles. It is widely used for military and civilian purposes including national defense, space science, medical diagnosis, etc. [4]-[10]. The MCP can be considered as a microporous plate with a regular hexagonal arrangement [11], [12]. Compared to the diameter of the MCP, the pore diameter is practically negligible. It is mostly composed of silicon dioxide (40-50 %), lead dioxide (20-30 %) and other metal compounds [13], which makes it susceptible to intense mechanical shocks. To ensure the safety and reliability of the MCP in the HERD, it is urgent to investigate its mechanical properties using the finite element method (FEM).

In terms of MCP, most of the existing studies focused on the investigation of its gain, time characteristics and other performances, such as the effect of cosmic particles on MCP [14], a method to improve the quantum efficiency of extreme ultraviolet MCP [15], the exploration of gain saturation [16], the investigation of MCP saturation/gain drop [17], [18], and the investigation of atomic layer deposited MCP [19]. In addition, the existing studies also investigated the frictional properties of MCP under the condition of crimping [20], the design of spring ring for MCP stack [21], the planeness of MCP [22], etc. Unfortunately, there are only a few studies to date that deal with the mechanical properties of MCP. Due to the microporous structure of MCP, the investigation of its mechanical properties is quite difficult. The mechanical properties of MCP, including strength and stiffness, fluctuate in a wide range when the geometric parameters and material

DOI: 10.2478/msr-2024-0023

*Corresponding author: baiyonglin@opt.ac.cn (Y. Bai) properties change. Therefore, it is important to study the mechanical properties of MCP and establish a mechanical model for MCP, which could help in the optimization of MCP for aerospace-grade detectors.

The main contributions of this study can be summarized as follows. To ensure the reliability and robustness of the MCP in space applications, the study of the mechanical properties of the MCP is particularly important. Considering that the MCP has millions of micro through-holes, it cannot be directly modeled by the FEM. Therefore, we proposed an equivalent mechanical model of an MCP using FEM, the effectiveness of which was verified by a sine sweep test using a laser Doppler vibrometer (LDV) to obtain an equivalent mechanical model of the MCPs with different geometric parameters. In the future, this study can help researchers to design and optimize MCP for space-grade detectors.

2. THEORY OF THE EQUIVALENT MODEL OF MCP

For ultra-thin microporous plates such as MCP, their mechanical properties can hardly be optimized and improved by direct modeling, which is why the equivalent mechanical model of MCP is absolutely necessary.

To solve the difficulty of creating a complete 3-dimensional (3D) model, the majority of researchers equate this structure with uniform pores to a solid. Among them, Slot and O'Donnell determined effective in-plane elastic constants with different ligament efficiencies for thick perforated plates with square and triangular penetration patterns, using the equal displacement method under generalized plane strain conditions [23]. Yang considered micro-pore optic (MPO) plates with millions of micro-square pores with a width of 20 µm as anisotropic uniform plates with the same properties, whereupon only the in-plane mechanical properties of MPO plates were estimated [24]. Baik used the average hole size to analyze the deformation behavior of the perforated sheet with non-uniform holes under uniaxial tension, and his study only concerned the apparent in-plane material properties of the sheet [25]. However, the in-plane and out-plane material properties of the perforated plates with triangular penetration patterns are sparse, and the effect of geometric parameters on the material properties has not been fully investigated.

Fig. 1 shows the MCP with a solid border and the equivalent mechanical model. The MCP with a solid border consists of a plate with millions of micro through-holes arranged in regular hexagons and a rim. The plate with millions of micro through-holes arranged in regular hexagons corresponds to an orthotropic solid with the same diameter, and the rim of the MCP is still the main material of the MCP. For the borderless MCP, the material property is orthotropic. Nevertheless, certain potential factors are not taken into consideration. These include the secondary electron emission layer, the conductive layer generated by hydrogen reduction and the effect of the bias angle on the strength of the MCP. The 3D Cartesian coordinate system is also defined in Fig. 1. The defined z-axis in Fig. 1(a) is perpendicular to the surface of the MCP, and the x-axis and y-axis in Fig. 1(a) are all parallel to the surface of the MCP. In Fig. 1(b), the Young's modulus in the x-direction E_x is parallel to the first main material direction - the x-axis, the Young's modulus in the y-direction E_y is parallel to the second main material direction - the y-axis, the Young's modulus in the z-direction E_z is parallel to the third main material direction - the z-axis. The origin in Fig. 1 is in the center of the surface of the MCP.

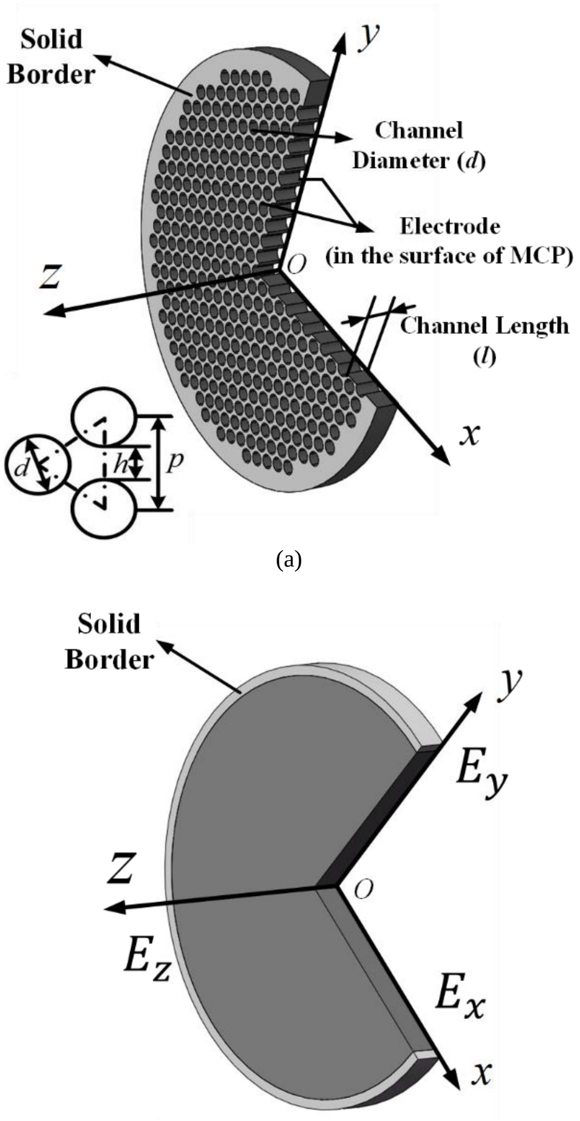

(a)

(b)

Fig. 1. (a) The schematic diagram of the MCP with a solid border, (b) The equivalent mechanical model of the MCP with a solid border.

3. RESULTS

A. *Acquiring material properties of main material of MCP*

Obtaining the material properties of the main materials of MCP is a prerequisite for creating an equivalent mechanical model of MCP. Since we do not know the material properties of MCP supplied by northern night vision (Nanjing), we first conducted tensile tests to determine the Young's modulus, Poisson's ratio, shear modulus and tensile strength. The Young's modulus E is the ratio of stress to strain per unit area of a material under tension or compression and can be expressed as

$$E = \frac{\sigma}{\varepsilon} = \frac{PL_0}{(L-L_0)A_0} \qquad (1)$$

where σ is the stress, ε is the strain, P is the load provided by the universal material testing machine, A_0 is the initial cross-sectional area, L_0 is the initial gauge length and L is the gauge length at a given point. The Poisson's ratio v refers to the ratio of the transverse normal strain to the axial normal strain of a material under uniaxial tension or compression. The shear modulus G is related to E and v and can be written as

$$G = \frac{E}{2(1+v)} \tag{2}$$

The tensile strength σ_b is the maximum load-bearing capacity of the material under static tension. For brittle materials, such as the base material of the MCP - lead glass - the tensile strength is the breaking strength of the material.

Table 1. Tensile test results of Type 1.

No.	Width [mm]	Thickness [mm]	Young's modulus [GPa]
1	25.10	2.99	60.77
2	25.08	3.04	65.87
3	24.99	2.81	65.75
Average	25.06	2.95	64.13

In accordance with the GB/T1040.1-2018 standard, two tensile specimens of different sizes are machined to obtain different material properties. The whole process of the tensile tests performed is shown in Fig. 2. In order to minimize the error caused by the tests, three identical specimens (referred to as Type 1) were used for the tests under the same conditions to obtain the Young's modulus (Fig. 2(a)). In Fig. 2(a), the two clamped parts of Type 1 are fixed in the universal testing machine and the biaxial extensometer is fixed on the Type 1, which is used to measure the deformation of the specimen, then, the universal testing machine starts stretching slowly and evenly until the tensile specimen breaks. Fig. 2(b) shows the condition when Type 1 breaks, and the gauge length of Type 1 is 100 mm. Six identical specimens (referred to as Type 2) were used for the tests under the same conditions to determine the Poisson's ratio (Fig. 2(c)). In Fig. 2(c), two uniaxial strain gauges arranged perpendicular to each other are used to measure transverse and axial strain, respectively. The gauge length of Type 2 is 50 mm.

Table 1 lists the results of the Young's modulus of Type 1, and the Young's modulus E of the main material of MCP is averaged as 64.13 GPa. Table 2 shows the results of Poisson's ratio and tensile strength, so $v = 0.27$, and $\sigma_b = 31.7$ MPa, respectively. According to (2), $G = 25.208$ GPa can be obtained.

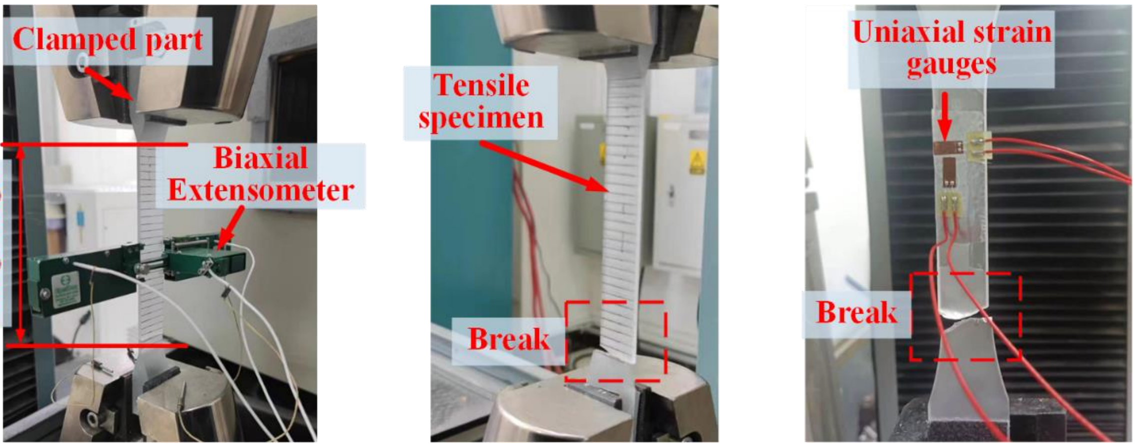

(a) (b) (c)

Fig. 2. (a) The experimental setup of the tensile test for the specimen Type 1, which can obtain the Young's modulus, (b) The image when Type 1 breaks the end of tensile tests, (c) The end of tensile test of Type 2.

Table 2. Tensile test results of Type 2.

No.	Width [mm]	Thickness [mm]	Poisson's ratio	Tensile strength [MPa]
1	15.16	4.18	0.294	42.826
2	15.06	4.16	0.296	35.995
3	15.04	4.34	0.259	28.721
4	15.01	4.16	0.176	26.163
5	15.08	4.13	0.202	23.390
6	15.04	4.18	0.406	33.400
Average	15.07	4.19	0.272	31.700

The main material of MCP is actually high lead silicate glass, and the approximate calculation equation for the Young's modulus of silicate glass can be expressed as

$$E = E_1P_1 + E_2P_2 + E_3P_3 + \cdots + E_nP_n \tag{3}$$

where $E_1, E_2, \cdots, E_n$ are the elasticity coefficients and $P_1, P_2, P_3, \cdots, P_n$ are the percentages of oxides. The Type 1 and Type 2 samples consist of approximately the compositions given in Table 3, so that the Young's modulus of MCP is approximately 63.082 GPa, which is comparable to the 64.13 GPa from the tensile test. The result proves that the data measured in the tensile test are credible.

Table 3. The composition and elasticity coefficient of MCP.

Composition	Percent [%]	Elasticity oefficient [GPa]
SiO_2	44.4	70
Al_2O_3	1.2	180
Na_2O	3.2	61
K_2O	6.5	40
PbO	25.0	46
Bi_2O_3	19.7	70

B. Establishing the equivalent mechanical model of MCP

In this study, we applied the FEM to obtain an equivalent model of the MCP, where the whole process can be approximated as the determination of the material properties of the equivalent model of the MCP. In the FEM, the force vector $\{F\}$ is equal to the stiffness matrix $[K]$ multiplied by the displacement vector $\{\delta\}$. The correlation between the stress vector $\{\sigma\}$ and the strain vector $\{\varepsilon\}$ can be written as

$$\{\sigma\} = [D]\{\varepsilon\} \tag{4}$$

where $[D]$ is the elasticity matrix. The stress state and the strain state at any position of an object can be determined by six stress components and six strain components, respectively. Therefore, in the Cartesian system, the stress vector and the strain vector can be described as

$$\{\sigma\} = [\sigma_x \quad \sigma_y \quad \sigma_z \quad \tau_{xy} \quad \tau_{yz} \quad \tau_{xz}]^T \tag{5}$$

and

$$\begin{aligned}\{\varepsilon\} &= [\varepsilon_x \quad \varepsilon_y \quad \varepsilon_z \quad \gamma_{xy} \quad \gamma_{yz} \quad \gamma_{xz}]^T \\ &= \left[\frac{\partial u}{\partial x} \quad \frac{\partial u}{\partial y} \quad \frac{\partial w}{\partial z} \quad \frac{\partial u}{\partial y}+\frac{\partial v}{\partial x} \quad \frac{\partial v}{\partial z}+\frac{\partial w}{\partial y} \quad \frac{\partial w}{\partial x}+\frac{\partial u}{\partial z}\right]^T\end{aligned} \tag{6}$$

where $\sigma_x, \sigma_y, \sigma_z$ are normal stresses, $\tau_{xy}, \tau_{yz}, \tau_{yz}$ are shear stresses, $\varepsilon_x, \varepsilon_y, \varepsilon_z$ are normal strains and $\varepsilon_{xy}, \varepsilon_{yz}, \varepsilon_{xz}$ are shear strains. For orthotropic materials, the elasticity matrix can be described as

$$[D] =$$

$$\begin{bmatrix} \frac{1-v_{yz}v_{zy}}{E_yE_z\Psi} & \frac{v_{xy}+v_{xz}v_{zy}}{E_xE_z\Psi} & \frac{v_{zx}+v_{yz}v_{zy}}{E_yE_z\Psi} & 0 & 0 & 0 \\ \frac{v_{xy}+v_{xz}v_{zy}}{E_yE_z\Psi} & \frac{1-v_{xz}v_{zx}}{E_xE_z\Psi} & \frac{v_{yz}+v_{yz}v_{xz}}{E_xE_y\Psi} & 0 & 0 & 0 \\ \frac{v_{zx}+v_{yz}v_{zy}}{E_yE_z\Psi} & \frac{v_{yz}+v_{yx}v_{xz}}{E_xE_y\Psi} & \frac{1-v_{xy}v_{yx}}{E_xE_y\Psi} & 0 & 0 & 0 \\ 0 & 0 & 0 & G_{xy} & 0 & 0 \\ 0 & 0 & 0 & 0 & G_{yz} & 0 \\ 0 & 0 & 0 & 0 & 0 & G_{xz} \end{bmatrix} \tag{7}$$

In the matrix,

$$\Psi = \frac{1-v_{xy}v_{yx}-v_{yz}v_{zy}-v_{zx}v_{xz}-2v_{xy}v_{yz}v_{zx}}{E_xE_yE_z} \tag{8}$$

According to the symmetry of the elasticity matrix, the conclusion is that

$$E_x v_{yx} = E_y v_{xy} \tag{9}$$

$$E_y v_{zy} = E_z v_{yz} \tag{10}$$

$$E_z v_{xz} = E_x v_{zx} \tag{11}$$

where E_x, E_y, E_z are the Young's modulus along the three principal axes, v_{xy}, v_{yz}, v_{xz} are Poisson's ratio and G_{xy}, G_{yz}, G_{xz} are the shear modulus.

When a system is in equilibrium, the work of the external force on the virtual displacement W_{out} is equal to the work of the internal force on the corresponding virtual displacement W_{in}, which is the principle of virtual work. And it can be written as

$$W_{in} = \{\delta\}^T \iiint \{B\}^T\{D\}\{B\}\{\delta\}dV \tag{12}$$

$$W_{out} = \{\delta\}^T\{F\} = \{\delta\}^T\{K\}\{\delta\} \tag{13}$$

where $\{B\}$ is the strain-displacement matrix varying with the element type, so that the stiffness matrix can be expressed as

$$[K] = \iiint \{B\}^T\{D\}\{B\}dV \tag{14}$$

It must be ensured that the force vector of the MCP is equal to that of the equivalent model and that the displacement of the MCP is equal to that of the equivalent model. When the element types are determined, the elasticity matrix of the equivalent model is obtained accordingly, in other words, the nine independent elastic constants of the equivalent model ($E_x^*, E_y^*, E_z^*, v_{xy}^*, v_{yz}^*, v_{xz}^*,\ G_{xy}^*, G_{yz}^*, G_{xz}^*$) are determined.

To obtain the nine elastic constants of the equivalent model, we chose an analysis model of six smallest units of the MCP in the *x*-direction and nine smallest units of the MCP in the *y*-direction in the numerical analysis, where the smallest unit of the MCP is defined as an independent honeycomb-like structure, as shown in Fig. 3(a). Therefore, for the equivalent model, the smallest unit can be defined as a regular hexagon with side length $p/\sqrt{3}$. To obtain the nine elastic constants of the equivalent model, the corresponding calculation methods are carried out as follows:

1. E_x^*: Under a 2-dimensional (2D) plane stress condition, a roller constraint is added as a boundary condition at the edge *Cx* of the selected part of the MCP, and a concentrated force F_x is applied at the edge *CFx* in the *x*-direction, as shown in Fig. 3(b). The Young's modulus is from Section 3, therefore the maximum displacement of the part of the MCP can be determined. Under the 2D plane stress condition, the orthotropic elasticity properties are pre-set, a roller constraint is added as the boundary condition at the edge *Cx** of the selected part of the MCP, and a concentrated force F_x is applied in the *x*-direction at the edge *CFx**, as shown in Fig. 3(e). The Young's modulus in the *x*-direction E_x^* is adjusted until the error between the maximum displacement of the MCP in the *x*-direction and the maximum displacement of the equivalent model in the *x*-direction is less than 1 %. Therefore, E_x^* can be obtained.

2. E^*_y, ν^*_{xy} and G^*_{xy}: Under the 2D plane stress condition, a roller constraint is added as a boundary condition at the edge *Cy* of the selected part of the MCP and a concentrated force F_y is applied in the *y*-direction at the edge *CFy*, as shown in Fig. 3(c). Under the 2D plane stress condition, the orthotropic elasticity properties are pre-set, a roller constraint is added as a boundary condition at the edge *Cy** of the selected part of the MCP, and a concentrated force F_y is applied in the *y*-direction at the edge *CFy**, as shown in Fig. 3(e). E^*_y is obtained when the maximum displacement of the MCP is approximately equal to that of the equivalent model in the *y*-direction. ν^*_{xy} is obtained when the maximum displacement of the MCP is approximately equal to that of the equivalent model in the *x*-direction. G^*_{xy} is obtained by

$$G^*_{xy} = \frac{E^*_{xy}}{2(1+\nu^*_{xy})} \qquad (15)$$

3. E^*_z, ν^*_{yz} and G^*_{xz}: The face *Sz* at the selected part of the MCP is fixed as the boundary condition and a concentrated force F_z is applied in the *z*-direction at the face *SFz*, as shown in Fig. 3(d). The face *Sz** on the equivalent model of the MCP is fixed as the boundary condition and a concentrated force F_z is applied in the *z*-direction at the face *SFz**, as shown in Fig. 3(f). Thus, E^*_y is obtained when the maximum displacement of the MCP is approximately equal to that of the equivalent model in the *z*-direction. ν^*_{xy} is obtained when the maximum displacement of the MCP is approximately equal to that of the equivalent model in the *y*-direction. G^*_{xy} is obtained when the maximum displacement of the MCP is approximately equal to that of the equivalent model in the *x*-direction.
4. G^*_{xz}: The face *Sz* at the selected part of the MCP is fixed as the boundary condition and a concentrated force F_{zx} is applied in the *x*-direction at the face *SFz*, so G^*_{xz} can be obtained when the maximum displacement of the MCP is approximately equal to that of the equivalent model in the *x*-direction.
5. G^*_{yz}: The face *Sz* at the selected part of the MCP is fixed as the boundary condition and a concentrated force F_{zy} is applied in the *y*-direction at the face *SFz*, so G^*_{yz} can be obtained when the maximum displacement of the MCP is approximately equal to that of the equivalent model in the *y*-direction.

Therefore, when there is a type of electrodeless MCP with a pore diameter of 6 µm and a thickness of 0.5 mm with an open area ratio of 60 %, the equivalent elastic constants are obtained as E^*_x = 4.02 GPa, E^*_y = 5.46 GPa, E^*_z = 25.68 GPa, ν^*_{xy} = 0.29, ν^*_{yz} = 0.055, ν^*_{xz} = 0.041, G^*_{xy} = 1.84 GPa, G^*_{yz} = 5.91 GPa, G^*_{xz} = 6.36 GPa.

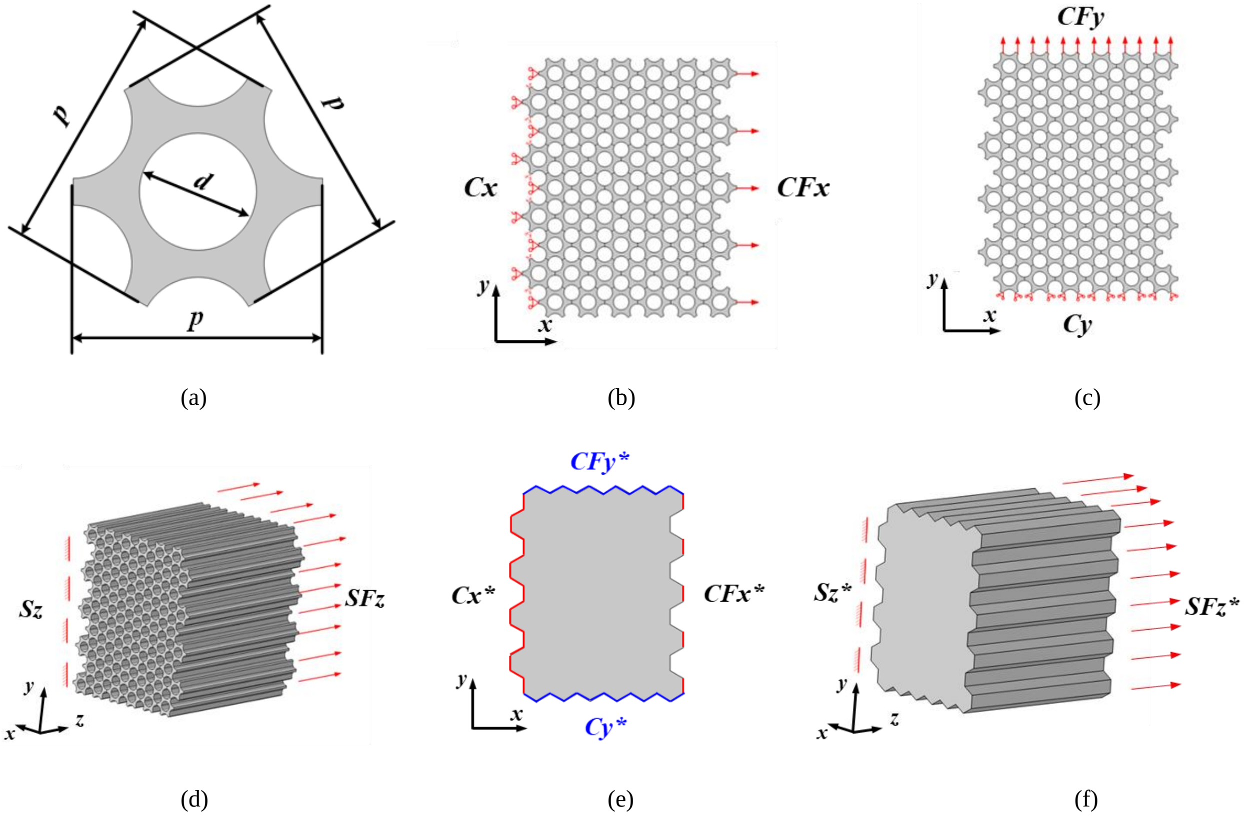

(a) (b) (c)

(d) (e) (f)

Fig. 3. (a) The smallest unit of the common MCP (top view). Schematic diagrams that show the analysis model of the MCP under plane stress in the (b) *x*-direction, in the (c) *y*-direction and (d) under the 3D analysis model of the MCP in the *z*-direction. Schematic diagrams that show the analysis model of the equivalent model of the MCP under plane stress (e) in the *x*-direction and *y*-direction and under the 3D analysis model of the equivalent model of the MCP in the (f) *z*-direction.

When the electrodes on the surface of the MCP are considered, the model is rebuilt as shown in Fig. 4. The material of the electrode is Ni80Cr20, its density is 8400 kg/m^3, the Young's modulus is 268.5 GPa and the Poisson's ratio is 0.303. The thickness of the electrode on the surface t_{NiCr} is 300 nm, the coating depth on the input surface xdi is 0.5 times the pore diameter, the coating depth on the output surface xdo is 2 times the pore diameter and the maximum thickness of the electrode in the inner wall of the channel t is 1.3 µm, and the analysis method is the same as the analysis of the electrodeless MCP. Consequently, for a type of MCP with a pore diameter of 6 µm, a thickness of 0.5 mm and an open area ratio of 60 %, the equivalent elastic constants are obtained as E_x^* = 4.40 GPa, E_y^* = 5.87 GPa, E_z^* = 25.69 GPa, υ_{xy}^* = 0.25, υ_{yz}^* = 0.062, υ_{xz}^* = 0.046, G_{xy}^*= 2.054 GPa, G_{yz}^*= 5.91 GPa, G_{xz}^*= 6.36 GPa.

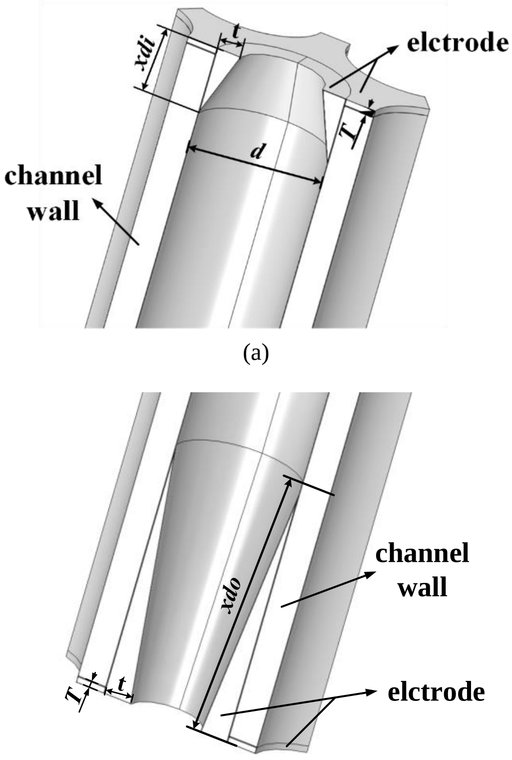

Fig. 4. Schematic diagrams demonstrating the electrodes of (a) the input surface and (b) the output surface of the MCP.

C. Verification of the equivalent mechanical model of MCP

To verify the accuracy of the equivalent mechanical model of the MCP, we selected two MCPs with an outer diameter of 50 mm, a thickness of 0.5 mm, a pore diameter of 6 µm, an open area ratio of 60 % and a solid edge diameter of 44 mm, numbered DY21080001-157C # 495 and UE5006. The selected DY21080001-157C # 95 is an MCP that can be directly mounted in the detector, but no electrodes are applied to the surface of sample UE5006. The schematic diagram and the front view of the verification system are shown in Fig. 5. A pressing ring with an inner diameter of 40 mm is used to fix the MCP in the vibrating fixture. The vibrating fixture is attached to the vibration exciter with several pressure plates and bolts, and an accelerometer is mounted on the vibrating fixture as a control point near the pressure ring. Since the weight of the MCP (approximately 2 g) is much lower than that of the accelerometer (approximately 10 g), we used a non-contact measuring device - the LDV - to measure the displacement of the MCP. The displacement resolution of the LDV we chose is 1 picometer, and the linear error is less than or equal to 1 %. The fiber laser head of the LDV is mounted on a tripod and must ensure that the laser hits the center of the upper surface of the MCP and that the fiber laser head is adjusted so that the signal light of the control box is as strong as possible. The MCP has a porous structure, therefore, when the laser shines directly on the MCP, some spots appear. In response to this situation, we stick a reflective film with a diameter slightly larger than the diameter (22 µm) of the laser spot in the center of the surface of the MCP.

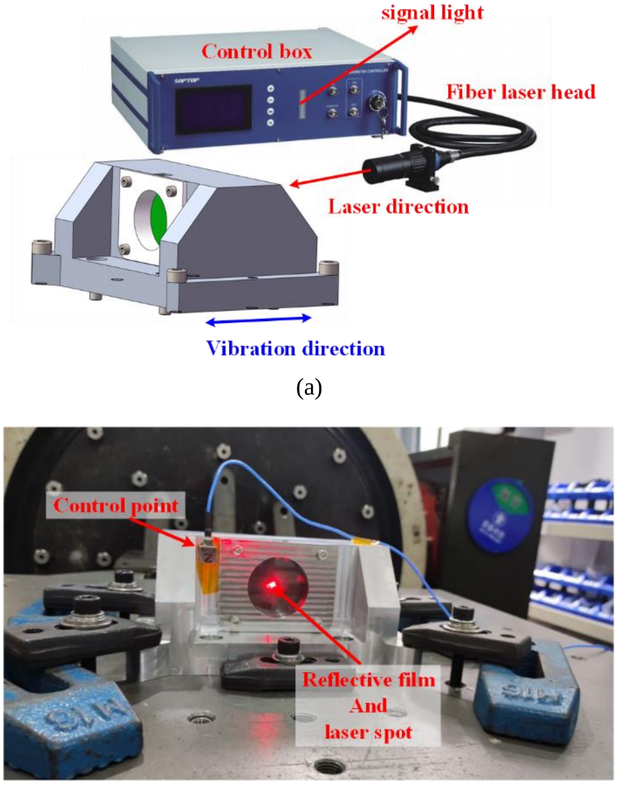

Fig. 5. (a) Schematic diagram of the verification system, (b) Front view of the verification system (on scene).

The vibration conditions provided by the vibration exciter are used for verification tests and harmonic response analysis (0.5 g between 10 Hz and 2000 Hz, with the sine sweep rate of 4 oct/min). The finite element model is modified several times to match the experimental results for which the material properties are taken from the previous section. The data provided by the LDV are the time-varying displacement values, while the data obtained by harmonic response analysis are the frequency-varying displacement values. To obtain the natural frequency of the MCP, the data provided by the LDV must be converted to the frequency domain.

During the sine sweep test, the frequency varies with time, so the characteristics of the data provided by the LDV are formulated as follows. First, the displacement decreases with time. Second, the curve obtained is sinusoidal. Third, the frequency increases logarithmically with time. Therefore, we perform a short-time Fourier transform (STFT) to convert the displacement values into frequency-domain data. Then we select an appropriate window size to perform a piecewise Fourier transform, after which a Flattop window is used to mitigate the leakage of the Fourier transform and correct the amplitude.

Fig. 6 shows the displacement curves of the sample DY21080001-157C # 495 measured with the LDV and calculated with the FEM. Since Fig. 7 shows the first two orders of the mode shapes of the validation system and their natural frequencies, only the first natural frequency exists in the frequency range from 5 Hz to 2000 Hz, with the peak at 1600 Hz caused by the perturbation of the vibration fixture. Table 4 shows the measured results and the FEM results of the two samples. Since all these errors are less than 10 %, the acceptability of the created equivalent mechanical model is thus conformed. Possible explanations for the errors are that there are slight differences in the boundary conditions and that there are slight differences in the contact methods between the simulation and the test.

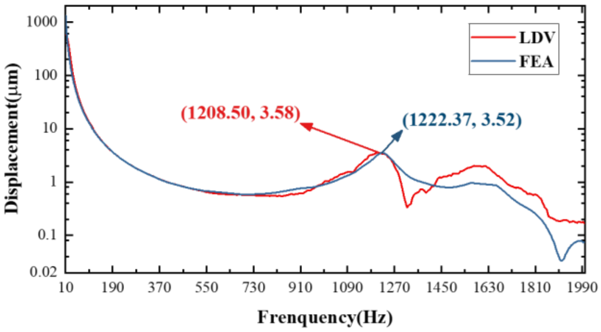

Fig. 6. The displacement curve measured by the LDV and the displacement curve of the sample DY21080001-157C # 495 obtained by FEM.

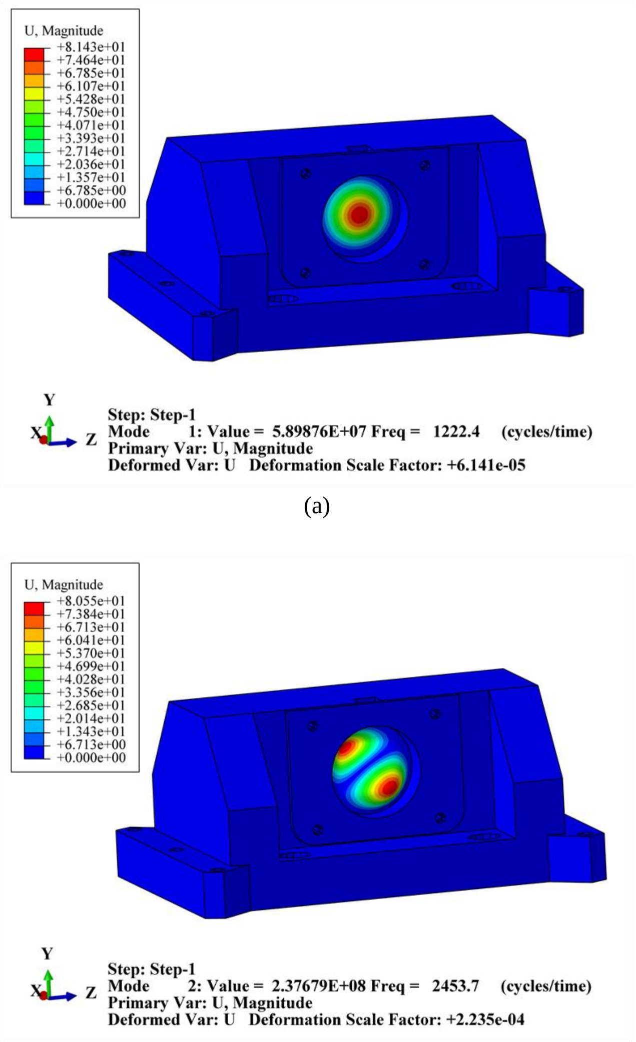

(a)

(b)

Fig. 7. (a) The first-order and (b) second-order mode shapes of the validation system.

Table 4. Comparison between the measured results and the FEM results.

Sample number	The 1st natural frequency [Hz]			Maximum amplitude [μm]		
	Measured	FEM	Error	Measured	FEM	Error
DY21080001-157C # 495	1208.50	1222.37	1.15 %	3.58	3.52	1.68 %
UE5006	1125.00	1193.65	6.10 %	3.95	3.60	8.86 %

Table 5. The effect of geometric parameters on material properties (OAR = 60 %, ρ = 1332.504 kg/m^3, effective area).

Pore diameter [μm]	E_x^* [GPa]	E_y^* [GPa]	E_z^* [GPa]	v_{xy}	v_{yz}	v_{xz}	G_{xy} [GPa]	G_{yz} [GPa]	G_{xz} [GPa]
6	4.40	5.87	25.69	0.25	0.062	0.046	2.054	5.91	6.36
8	4.96	6.87	25.70	0.26	0.073	0.052	2.35	2.69	6.14
10	5.42	7.02	25.68	0.27	0.078	0.055	2.45	5.33	6.04
12	5.70	7.10	25.72	0.28	0.079	0.063	2.50	5.14	5.85

D. Parametric studies of the MCPs considering different geometric parameters

A complete MCP contains several major independent geometric parameters, namely the pore diameter d, the open area ratio OAR, the thickness of the plate l, the outer diameter D and the rim of the plate D_b. To create the equivalent model of the MCP, these geometric parameters are explained as follows.

a. The OAR of the ordinary MCP is generally 60 %. The detection efficiency of the MCP can be improved by using an MCP with funnel-type openings, so that the main OAR of the MCP remains unchanged and the effect of the funnel is minimized.
b. The material of the equivalent model varies in the diameter direction, but does not increase or decrease in the thickness direction compared to the MCP. Therefore, the material properties of the equivalent model of the MCP do not vary with the thickness of the MCP.
c. The overall dimension of the equivalent model is the same as that of the MCP, so that the outer diameter D and the rim of the plate D_b have no influence on the material properties of the equivalent model.

Hence, the elastic constants of the equivalent mechanical model of the MCP correlate only with the pore diameter.

By applying the control variable method and FEM, we obtained the elastic constants of the equivalent model with pore diameters of 6 µm, 8 µm, 10 µm and 12 µm, as shown in Table 5. The material properties for equivalent models of the MCPs with other pore diameters can be determined by interpolation.

4. DISCUSSION & CONCLUSION

In this study, considering the requirements of the HERD facility, the vulnerability of the MCP and its inability to withstand large shocks, we propose an equivalent mechanical model of the MCP. When creating the equivalent model, a special analysis model and boundary conditions are chosen to apply the FEM and minimize the errors. Then we design a corresponding system to verify the effectiveness of the equivalent model by sine sweep tests using the. The results show that the error of the harmonic response analysis and the test result is less than 10 %, which is acceptable. The equivalent mechanical model of the MCP with different pore diameters is obtained using the control variable method and FEM, in other words, the in-plane and out-plane material properties are all determined.

The equivalent mechanical model can be used to model the detectors with MCP stacks. This model is suitable for MCP with different materials, such as silicon or borosilicate glass. Furthermore, the application of this model can be extended to periodic structures that cannot be modeled directly, such as optical fiber panels. Furthermore, the model is suitable for the design and optimization of the MCP for aerospace-grade detectors.

Despite the aforementioned achievements, certain shortcomings must be pointed out, which are that the equivalent mechanical model is only applicable to MCPs with circular holes. Our future research will focus on improving the reliability and robustness of the MCP for aerospace-grade detectors and other detectors and lay the theoretical foundations for the continuous study of the MCP and its adaptability in the aerospace field.

ACKNOWLEDGMENT

This work was supported by National Natural Science Foundation of China under Grant No. 12027803.

REFERENCES

[1] Huang, X., Lamperstorfer, A. S., Sming Tsai, Y.-L., Xu, M., Yuan, Q., Chang, J., Dong, Y.-W., Hu, B.-L., Lü, J.-G., Wang, L., Wu, B.-B., Zhang, S.-N. (2016). Perspective of monochromatic gamma-ray line detection with the high energy cosmic-radiation detection (HERD) facility onboard China's space station. *Astroparticle Physics*, 78, 35-42. https://doi.org/10.1016/j.astropartphys.2016.02.003

[2] Xu, M., HERD collaboration. (2016). The high energy cosmic radiation facility onboard China's space station. *Nuclear and Particle Physics Proceedings*, 279-281, 161-165. https://doi.org/10.1016/j.nuclphysbps.2016.10.023

[3] Betti, P., Adriani, O., Antonelli, M., Bai, Y., Bai, X., Bao, T. et al. (2022). Photodiode read-out system for the calorimeter of the HERD experiment. *Instruments*, 6 (3), 33. https://doi.org/10.3390/instruments6030033

[4] Guest, A. J. (1971). A computer model of channel multiplier plate performance. *Acta Electronica*, 14 (1), 79-97. https://psec.uchicago.edu/Papers/Guest.pdf

[5] Wiens, R. C., Maurice, S., Robinson, S. H., Nelson, A. E., Cais, P., Bernardi, P. et al. (2021). The SuperCam instrument suite on the NASA Mars 2020 Rover: Body unit and combined system tests. *Space Science Reviews*, 217 (4). https://doi.org/10.1007/s11214-020-00777-5

[6] Chen, L., Wang, X., Tian, J., Zhao, T., Liu, C., Liu, H., Wei, Y., Sai, X., Wang, X., Sun, J., Si, S., Chen, P., Tian, L., Hui, D., Guo, L. (2017). The gain and time characteristics of microchannel plates in various channel geometries. *IEEE Transactions on Nuclear Science*, 64 (4), 1080-1086. https://doi.org/10.1109/TNS.2017.2676010

[7] Wehmeijer, J., van Geest, B. (2010). Image intensification. *Nature Photonics*, 4 (3), 152-153. https://doi.org/10.1038/nphoton.2010.21

[8] Shi, P., Jia, J., Zhang, Y., Zhang, B., Huang, Y., Jiao, P., Huang, K., Feng, Y., Wang, S. (2020). Advances in theoretical models and simulation of electron gain in microchannel plates. In *Second Target Recognition and Artificial Intelligence Summit Forum*. SPIE 11427, 1142736. https://doi.org/10.1117/12.2552917

[9] Sanctorum, J. G., Adriaens, D., Dirckx, J. J. J., Sijbers, J., van Ginneken, C., Aerts, P., Van Wassenbergh, S. (2019). Methods for characterization and optimisation of measuring performance of stereoscopic x-ray systems with image intensifiers. *Measurement Science and Technology*, 30 (10), 105701. https://doi.org/10.1088/1361-6501/ab23e7

[10] Nittoh, K., Konagai, C., Noji, T., Miyabe, K. (2009). New feature of the neutron color image intensifier. *Nuclear Instruments and Methods in Physics Research Section A: Accelerators, Spectrometers, Detectors and Associated Equipment*, 605 (1-2), 107-110. https://doi.org/10.1016/j.nima.2009.01.136

[11] Dolan, K. W. (1978). *Preliminary studies of microchannel plate photomultiplier tube neutron detectors for flight test applications*. Sandia Laboratories Livermore, SAND78-8266. https://www.osti.gov/servlets/purl/6207249

[12] Pan, J., Lv, J., Zhang, Z., Sun, J., Su, D. (2010). Ion feedback suppression for microchannel plate applied to third generation image intensifiers. *Chinese Journal of Electronics*, 19 (4), 757-762. https://doi.org/10.23919/CJE.2010.10168771

[13] Zhu, X., Guo, J., Cao, W., Liu, L., Zhang, G., Sun, X., Zhao, W., Si, J. (2020). Theoretical and experimental investigation of secondary electron emission characteristics of ALD-ZnO conductive films. *Journal of Applied Physics*, 128, 065102. https://doi.org/10.1063/5.0014590

[14] Gemer, A. J., Sternovsky, Z., James, D., Horanyi, M. (2020). The effect of high-velocity dust particle impacts on microchannel plate (MCP) detectors. *Planetary and Space Science*, 183, 104628. https://doi.org/10.1016/j.pss.2018.12.011

[15] Hemphill, R., Edelstein, J. (2003). Chemical method to increase extreme ultraviolet microchannel-plate quantum efficiency. II. Analysis and optimization. *Applied Optics*, 42 (13), 2251-2256. https://doi.org/10.1364/AO.42.002251

[16] Xie, Y., Zhang, Y., Wang, X., Sun, X. (2017). Research on the gain saturation effect of an image intensifier based on microchannel plate. *Infrared and Laser Engineering*, 146 (10), 1003005. https://doi.org/10.3788/irla201746.1003005

[17] Kobayashi, H., Hondo, T., Toyoda, M. (2021). Evaluation of microchannel plate gain drops caused by high ion fluxes in time-of-flight mass spectrometry: A novel evaluation method using a multi-turn time-of-flight mass spectrometer. *Journal of Mass Spectrometry*, 56 (3), e4706. https://doi.org/10.1002/jms.4706

[18] Kobayashi, H., Hondo, T., Kanematsu, Y., Suyama, M., Toyoda, M. (2023). Evaluation of transient gain-drop and following recovery property on microchannel plate: Comparison between two evaluation methods. *Nuclear Instruments and Methods in Physics Research Section A: Accelerators, Spectrometers, Detectors and Associated Equipment*, 1053, 168355. https://doi.org/10.1016/j.nima.2023.168355

[19] Ertley, C., Siegmund, O., Cremer, T., Craven, C., Minot, M., Elam, J., Mane, A. (2018). Performance studies of atomic layer deposited microchannel plate electron multipliers. *Nuclear Instruments and Methods in Physics Research Section A: Accelerators, Spectrometers, Detectors and Associated Equipment*, 912, 75-77. https://doi.org/10.1016/j.nima.2017.10.050

[20] Marckwordt, M., Lampton, M. (2000). Frictional properties of microchannel plates and common detector materials. *Review of Scientific Instruments*, 71 (4), 1906-1908. https://doi.org/10.1063/1.1150561

[21] Marckwordt, M. (2003). Development of a spring ring for microchannel plate stack fastening in the cosmic hot interstellar plasma spectrometer detector. *Review of Scientific Instruments*, 74 (1), 212-217. https://doi.org/10.1063/1.1527204

[22] Zhao, R., Huang, Y., Wang, J., Sun, Y., Huang, K., Zhou, Y., Wang, Y., Fu, Y. (2019). Image-spherizing-based planeness detecting method for a micro-channel plate. *Applied Optics*, 58 (3), 554-560. https://doi.org/10.1364/AO.58.000554

[23] Slot, T., O'Donnell, W. J. (1971) Effective elastic constants for thick perforated plates with square and triangular penetration patterns. *Journal of Engineering for Industry*, 93 (4), 935-942. https://doi.org/10.1115/1.3428087

[24] Yang, X., Zhang, C., Ling, Z., Jin, G., Li, L., Yuan, W., Zhang, S. (2018). The finite element analysis modeling of micro pore optic plate. In *Space Telescopes and Instrumentation 2018: Ultraviolet to Gamma Ray*. SPIE 10699, 106993Z. https://doi.org/10.1117/12.2312382

[25] Baik, S. C., Oh, K. H., Lee, D. N. (1996). Analysis of the deformation of a perforated sheet under uniaxial tension. *Journal of Materials Processing Technology*, 58 (2-3), 139-144. https://doi.org/10.1016/0924-0136(95)02096-9

Received January 25, 2024
Accepted August 26, 2024